[Supplementary information]

Phase-change mechanism and role of each element in Ag-In-Sb-Te: chemical bond evolution

Dasol Kim[a,b], Taek Sun Jung[a], Hanjin Park[c], Wonjun Yang[a,b], Jeonghwa Han[a,b], Soobin Hwang[a,b], Kyung Ik Sim[a], Young-Kyun Kwon[c], Jae Hoon Kim[a], and Mann-Ho Cho[a,b]*

[a]Department of Physics, Yonsei University, Seoul 03722, Republic of Korea

[b]Atomic-scale Surface Science Research Center, Yonsei University, Seoul 03722, Republic of Korea

[c]Department of Physics and Research Institute for Basic Sciences, Kyung Hee University, Seoul, 02447, Republic of Korea

* Corresponding author: mh.cho@yonsei.ac.kr

The supplementary information provides additional information to accompany that in the article. It is classified into four parts: I. X-ray photoelectron spectroscopy (XPS), II. density functional (DF) simulations, III. infrared spectroscopic ellipsometry (IR-SE), IV Hysteresis of electrical resistance on temperature (R-T), V. Scheme, and VI. Structural analysis (Raman and X-ray diffraction). In I. XPS, Supplementary Figure S1 shows core level spectroscopic details of Ag, In, Sb, and Te in amorphous and crystalline $In_5Sb_{77}Te_{18}$ (IST), $Ag_5Sb_{77}Te_{18}$ (AST), $Ag_4In_4Sb_{75}Te_{18}$ (AIST), and $Ag_4In_4Sb_{61}Te_{31}$ ($AIST_{Eutectic}$). In II. DF simulations, Supplementary Figures S2, S3, and S4 show snapshots of the atomic distributions, radial distribution function (RDF), and specific angle distribution function (ADF), respectively, of the amorphous and crystalline AIST structures reproduced by DF simulation. In III. IR-SE, Supplementary Figure S5 and Supplementary Table S6 provide details of the IR-SE spectra and fitting parameters, respectively, of $Sb_{80}Te_{20}$ (ST), AIST, $AIST_{Eutectic}$, AST, and IST. In IV. Supplementary Figure S7 and S8 provides resistance dependence on temperature of ST, AST, and AIST varying ramping rates and activation energy obtained from Kissinger and Arrhenius model, respectively. In V., Supplementary Figure S9 provides a scheme which states local environments of Ag-In-Sb-Te. In VI., Supplementary Figure S10 provides structural analysis for amorphous and crystalline AIST.

I. X-ray photoelectron spectroscopy

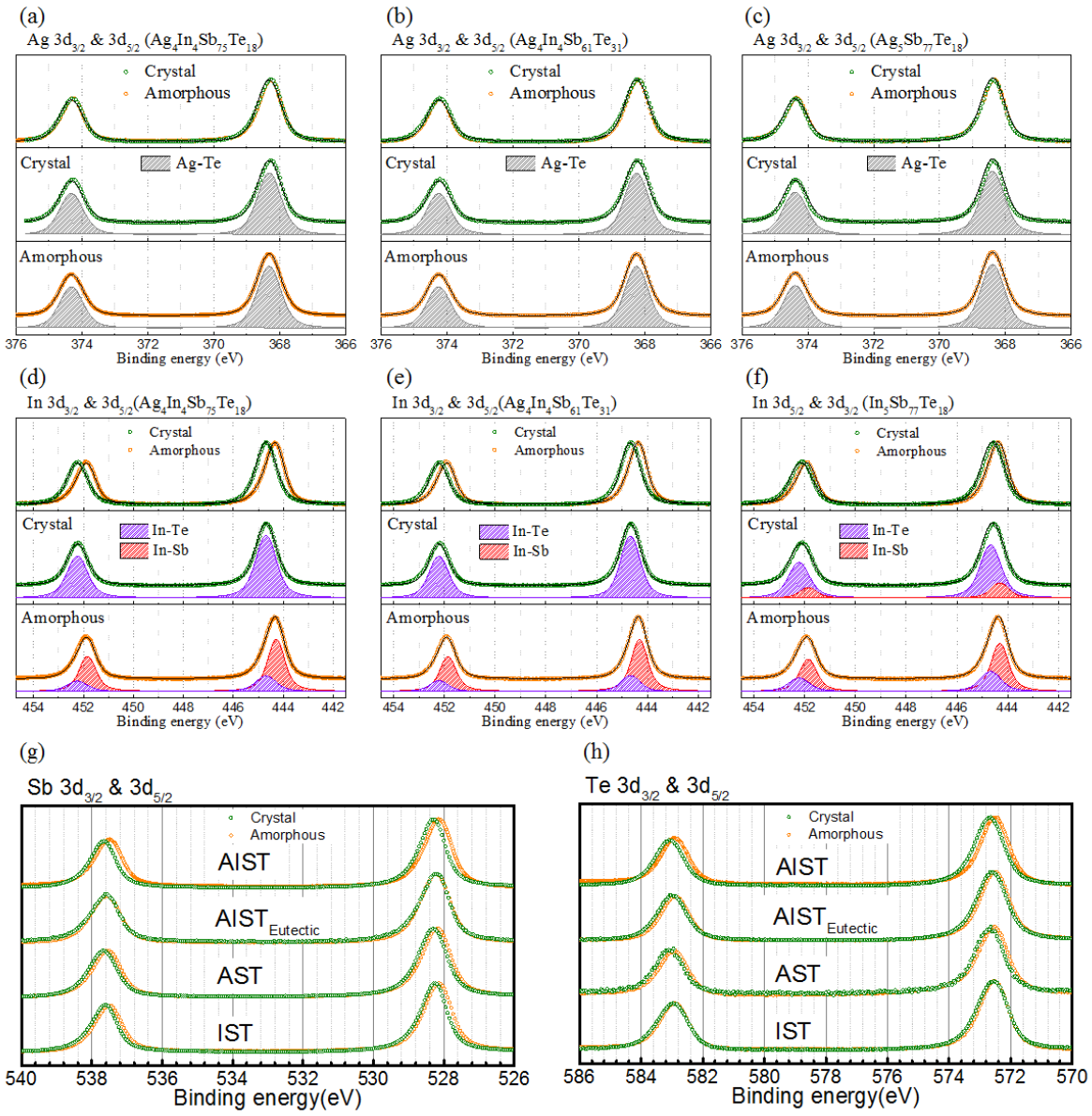

Supplementary Figure S1 Deep core level spectroscopy of $3d_{3/2}$ and $3d_{5/2}$ of (a)-(c) Ag, (d)-(f) In, (g) Sb, (h) Te in AIST, $AIST_{Eutectic}$, AST, and IST. (a)-(f) Measured data and fitting lines are shown in the form of a set of circles and black lines, respectively, where the crystalline (amorphous) data are coloured green (orange). In the upper panel, the measured data and fitting lines of both the crystalline and amorphous phases are shown simultaneously for comparison. In the middle (lower) panel, the measured data and fitting lines of the crystalline (amorphous) phases are shown with deconvoluted spectra. The spectra for the Ag-Te, In-Te, and In-Sb bonds are shown in silver, purple, and red, respectively. (g)-(h) Measured data are shown in the form of a set of circles, where the crystalline and amorphous data are shown in green and orange, respectively.

Spectral results corresponding to O 1s, whose binding energy is in the range of 533~531 eV,

could not be found in any films, indicating that the films are not oxidised. To confirm whether the samples are sufficiently crystallised, we additionally measured samples after annealing the crystalline films again at a temperature higher than the crystallisation temperature. Furthermore, to confirm whether the obtained data represent bulk or surface properties, we measured samples by varying the sampling depth by tilting the samples from 45° to 80° with respect to the detector. We concluded that the obtained data represent the bulk properties without the oxidised state, where the crystallinity of crystalline samples is sufficient.

The FWHM of $3d_{5/2}$ core level spectra of Te in IST, AST, AIST, and $AIST_{Eutectic}$ are wider than those of Ag, In, and Sb, which is the result of the various types of chemical bonding of Te compared with Ag, In, and Sb. These results are consistent with our suggestion that Te functions as a connection centre of chemical bonds. Further, as shown in Figure S2d and S2e, the spectral peaks of the element In of crystal $AIST_{Eutectic}$ are slightly narrower than those of crystalline AIST, which is the result of the abundance of Te in $AIST_{Eutectic}$. This abundance of Te in $AIST_{Eutectic}$ facilitates the formation of the $AgInTe_2$-like bonding topology by Ag and In in comparison with AIST.

II. Density functional theory

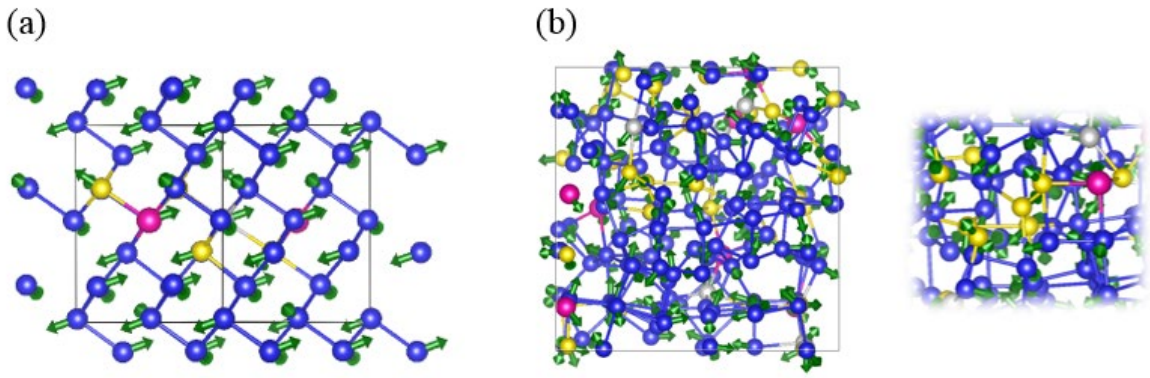

Supplementary Figure S2 Snapshot of atomic distributions for the crystalline $Ag_1In_1Sb_{18}Te_4$ cell and amorphous $Ag_8In_8Sb_{144}Te_{32}$ supercell at 300 K obtained by molecular dynamics (MD) simulations. (a) Cell of crystalline $Ag_1In_1Sb_{18}Te_4$ and (b) supercell of amorphous $Ag_8In_8Sb_{144}Te_{32}$, where atoms of Ag, In, Sb, and Te are grey, magenta, blue, and orange, respectively, and the sum of the three vectors indicating short bonds is shown in green.

To visualise the degree of ordering of each atom to show the alignment with adjacent atoms, a green arrow is utilised to represent the vector sum of three vectors defined from the adjacent atoms that form short bonds to the target atom. In the crystal, the vectors are well aligned, whereas those in the amorphous structure are disordered, which is consistent with the bond-interchange model[1].

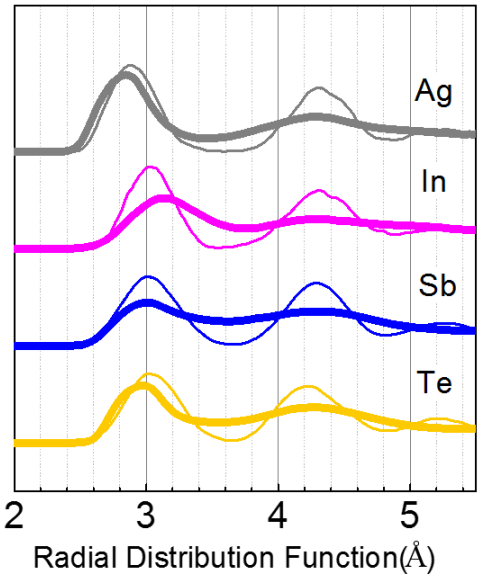

Supplementary Figure S3 Structural analysis of crystalline and amorphous cell reproduced by DFT. The radial distribution functions (RDFs) of the amorphous and crystalline structures are shown in thick and thin lines, respectively, where the RDF spectra of Ag, In, Sb, and Te are shown in grey, magenta, blue, and yellow, respectively.

To analyse the structural characteristics of the local environment of each element in the amorphous and crystalline states, we evaluated the radial distribution functions (RDFs) from the results obtained by our molecular dynamics simulations performed at $T = 300$ K, within canonical ensembles, as shown in Supplementary Figure S3. The bond lengths of Ag, In, Sb, and Te in the crystal structure were approximately 3 Å, which is consistent with the report that Ag, In, Sb, and Te in crystalline AIST randomly occupy sites of the A7 crystal structure where the bond lengths are 3 Å.[2] The bond length of Ag was slightly shorter than those of the other elements because of the donation of the peripheral electron for bonding and the reduction of the electron shell in comparison with Sb and Te. This is consistent with the report that Ag forms ionic bonds in the Ag-In-Sb-Te system.[3] Even in the amorphous structure, the bond lengths of Ag, Sb, and Te were similar to those in the crystal structure because the atomic displacements of elements in the crystallisation of AIST were relatively small compared with GST.[1] In contrast, the bond lengths of In in the amorphous structure increased in comparison to those of the crystalline structure to 3.2 Å; that is, the bonds are 7 % longer than those in crystalline AIST. This is consistent with our suggestion that the transition of the local environment of In is drastic upon the crystallisation of AIST in comparison with the environments of the other elements (Ag, Sb, and Te).

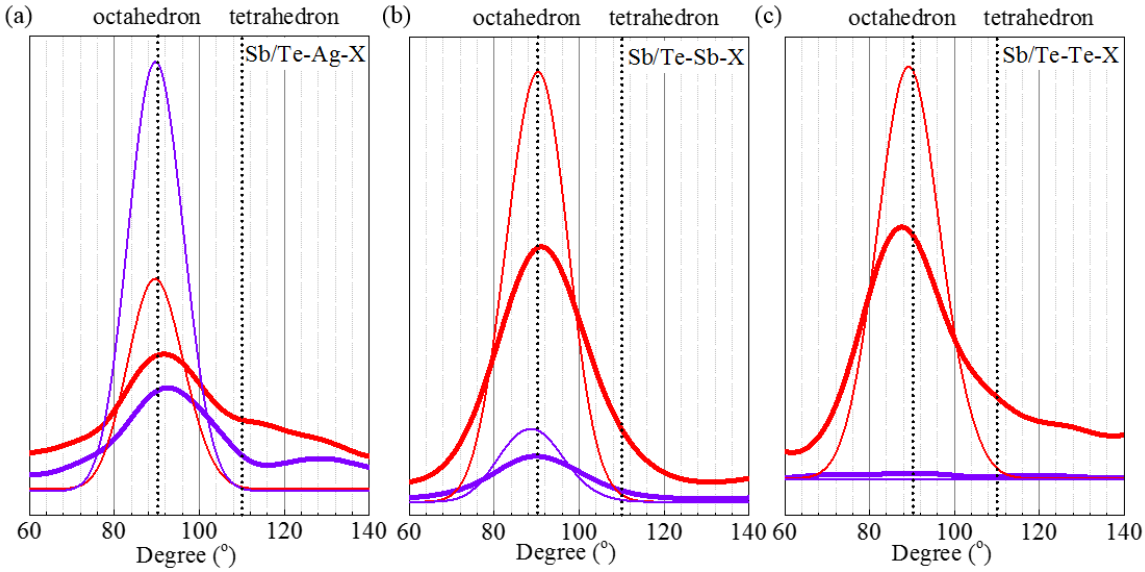

Supplementary Figure S4 Specific angle distribution functions of the crystalline and amorphous cell. The specific angle distribution function of the elements (a) Ag, (b) Sb, and (c) Te in the amorphous and crystalline structures are represented in thick and thin lines respectively, where the spectra of the angle representing Sb-Y-X are shown in red, and Te-Y-X in purple, respectively. Y represents the elements (a) Ag, (b) Sb, and (c) Te and X represents any elements in the structure.

The specific angle distribution functions of Ag, Sb, and Te in both the amorphous and crystalline structures are centred at 90°, which are different from those of In in the amorphous structure. This is consistent with our suggestion that the structural distortions of the element In in amorphous AIST are larger than those in crystalline AIST. The specific angle distribution functions of Te-Te-X, where X represents any element in the structure, of the amorphous and crystalline structure are negligibly small, which is consistent with our result that Te bonds with Ag, In, and Sb but not with Te itself.

III. Infrared-spectroscopic ellipsometry

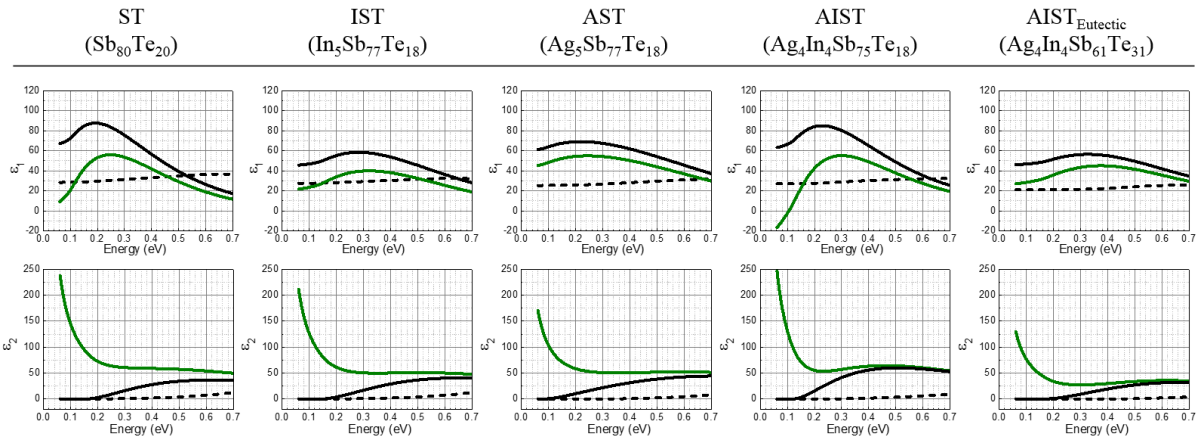

Supplementary Figure S5 Ellipsometry spectra of $Sb_{80}Te_{20}$(ST), $In_5Sb_{77}Te_{18}$(IST), $Ag_5Sb_{77}Te_{18}$(AST), $Ag_4In_4Sb_{75}Te_{18}$(AIST), and $Ag_4In_4Sb_{61}Te_{31}$($AIST_{Eutectic}$). Dielectric functions of amorphous and crystalline phase-change materials obtained with infrared spectroscopy ellipsometry are represented by the dashed black line and solid green line, respectively, whereas those of crystal phase-change materials without the Drude contribution are represented by the solid black line.

Supplementary Table S6 Fitting parameters of spectroscopic ellipsometry spectra of ST, IST, AST, AIST, and $AIST_{Eutectic}$. The fitting parameters including the Drude contribution and Tauc-Lorentz contribution are provided in Supplementary Table S5.

		ϵ_∞ (-Drude) @0.06eV	Drude			Tauc-Lorentz				
			ω_p (eV)	γ (eV)	σ_{DC} ($\Omega^{-1}cm^{-1}$)	A (eV)	C (eV)	E_0 (eV)	$\epsilon_{\infty\ T\text{-}L}$	E_g (eV)
Amorphous	$Sb_{80}Te_{20}$(ST)	28.3				30.5	0.6	1.0	12.2	0.2
	$In_5Sb_{77}Te_{18}$(IST)	27.4				13.6	0.5	0.9	19.3	0.2
	$Ag_5Sb_{77}Te_{18}$(AST)	25.3		-		35.1	0.9	1.1	14.4	0.3
	$Ag_4In_4Sb_{75}Te_{18}$(AIST)	26.8				44.4	1.4	1.4	12.1	0.2
	$Ag_4In_4Sb_{61}Te_{31}$($AIST_{Eutectic}$)	21.0				27.6	1.2	0.8	24.5	0.4
Crystal	$Sb_{80}Te_{20}$(ST)	67.1	1.7	0.2	1859.4	114.8	1.4	0.6	14.0	0.1
	$In_5Sb_{77}Te_{18}$(IST)	45.6	2.7	0.5	1760.2	93.5	1.7	0.8	11.0	0.1
	$Ag_5Sb_{77}Te_{18}$(AST)	61.3	2.7	0.7	1415.1	94.5	2.1	1.1	10.2	0.1
	$Ag_4In_4Sb_{75}Te_{18}$(AIST)	63.1	1.8	0.2	2241.3	115.2	1.3	0.6	20.6	0.1
	$Ag_4In_4Sb_{61}Te_{31}$($AIST_{Eutectic}$)	46.1	1.8	0.4	1092.0	60.3	1.2	0.7	25.9	0.1

As shown in the main manuscript, the bonding types of amorphous and crystalline ST, IST, AST, AIST, and $AIST_{Eutectic}$ are covalent and metavalent, respectively. In particular, the ϵ_∞ values of amorphous and crystalline $AIST_{Eutectic}$ are lower than those of ST, AST, and AIST, respectively, indicating that the atomic middle range ordering (AMRO) of amorphous and crystal $AIST_{Eutectic}$ is relatively deficient, which results from the lack of Sb in $AIST_{Eutectic}$ in comparison with ST, AST, and AIST. Specifically, the lack of Sb in $AIST_{Eutectic}$ induces a slight phase separation that disturbs the AMRO.[4] However, the % increase in ϵ_∞ of $AIST_{Eutectic}$ has a value comparable to those of ST, AST, and AIST.

The optical bandgaps of amorphous and crystalline ST, IST, AST, AIST, and $AIST_{Eutectic}$ are also shown in ϵ_2 in Supplementary Figure S1 and Supplementary Table S1. The optical bandgaps without the Drude contribution of amorphous (crystalline) ST, IST, AST, AIST, and $AIST_{Eutectic}$ are in the range of 0.3~0.5 eV (0.05~0.2 eV), which is consistent with published reports.[5] \

IV. Hysteresis of electrical resistance on temperature (R-T)

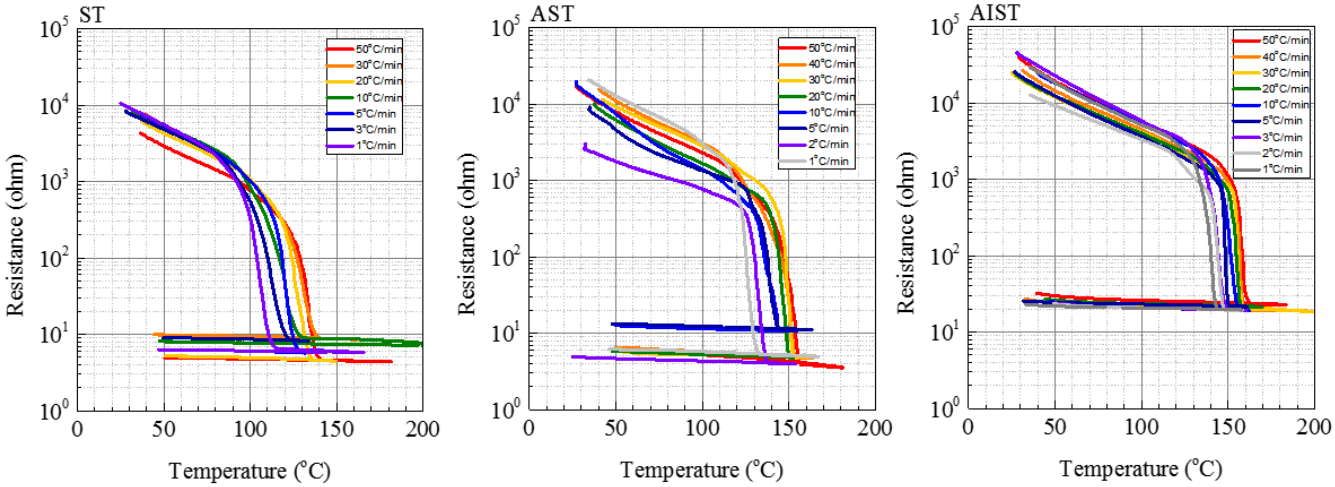

Supplementary Figure S7. Resistance dependence on temperature during annealing cooling of $Sb_{80}Te_{20}$(ST), $Ag_5Sb_{77}Te_{18}$(AST), $Ag_4In_4Sb_{75}Te_{18}$(AIST) varying ramping rate.

Decrease of electrical resistance on annealing from room temperature, negative temperature coefficient of resistance (TCR), is commonly found in ST, AST, and AIST films, i.e., amorphous phase represents semiconducting or insulating behavior rather than metallic behavior on annealing.[6] On cooling after crystallization, resistance of ST, AST, and AIST films negligibly changes on cooling. It indicates that conducting behavior of carriers in crystal film is differentiated with that of amorphous film.

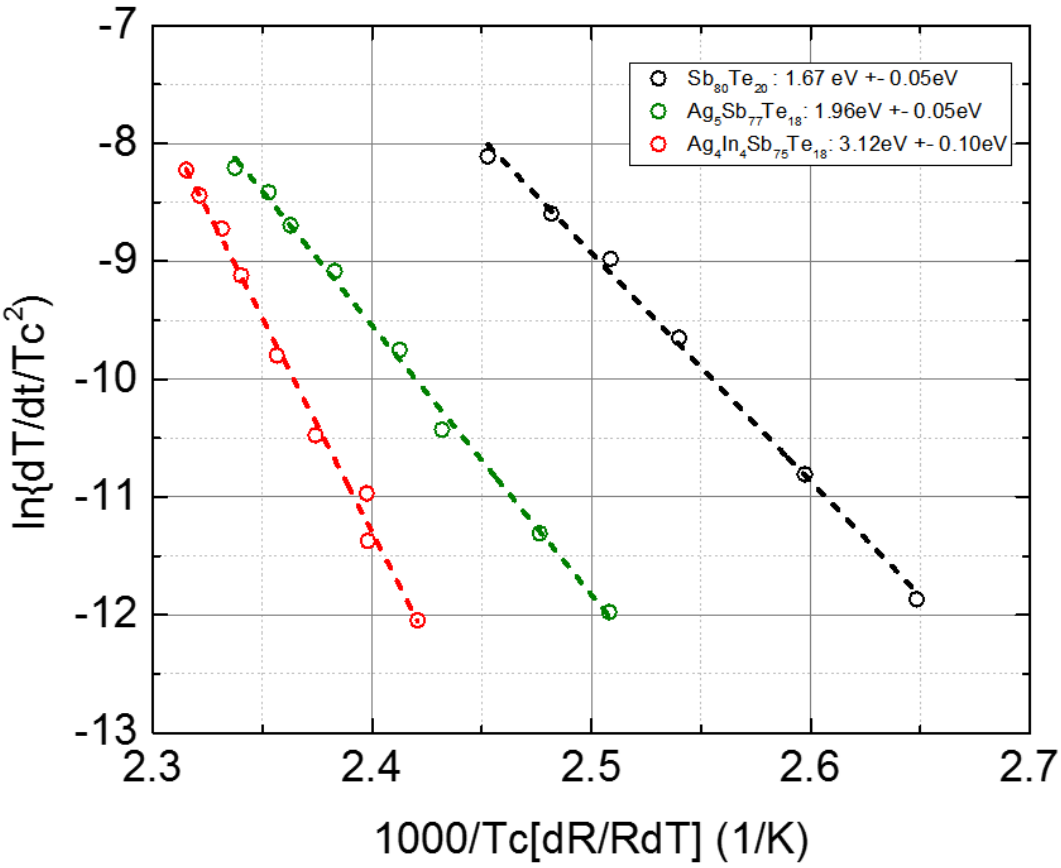

Supplementary Figure S8. Plotting based on Kissinger and Arrhenius model to obtain activation energy for crystallization.

V. Scheme

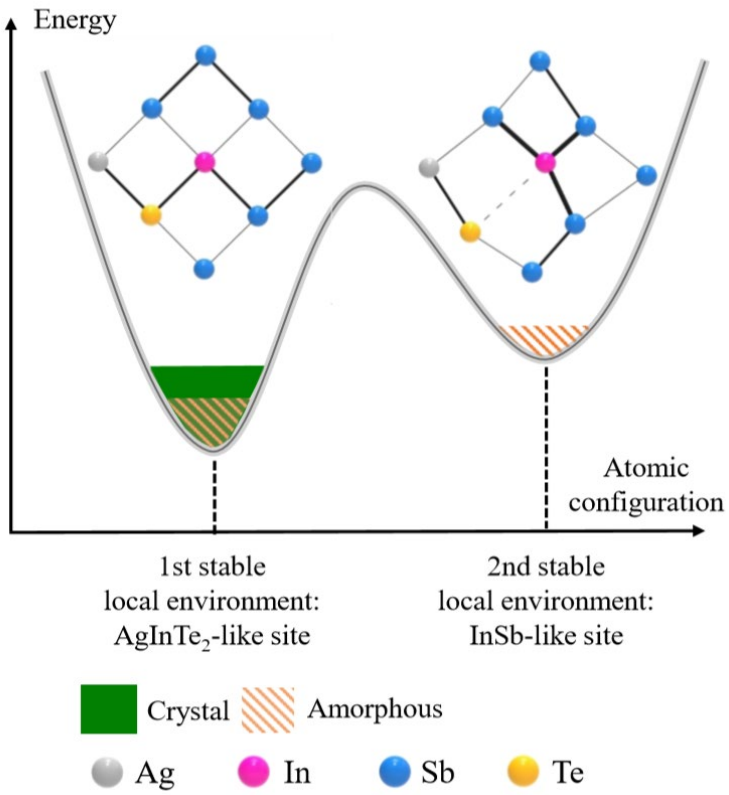

Supplementary Figure S9. Local environments of Ag-In-Sb-Te. Local environments of PCMs can be classified into energetically 1st and 2nd stable local environments. The local environment of crystalline PCMs consists of a 1st stable local environment, whereas those of amorphous PCMs consist of both 1st and 2nd stable local environments. The crystallization and amorphization of PCMs are deployed by the local environment transitions of certain element that differ considerably from the continuous random network model. Our results show that 1st and 2nd stable local environments of Ag-In-Sb-Te are $AgInTe_2$-like and InSb-like site, respectively.

VI. Structural analysis (Raman and X-ray diffraction)

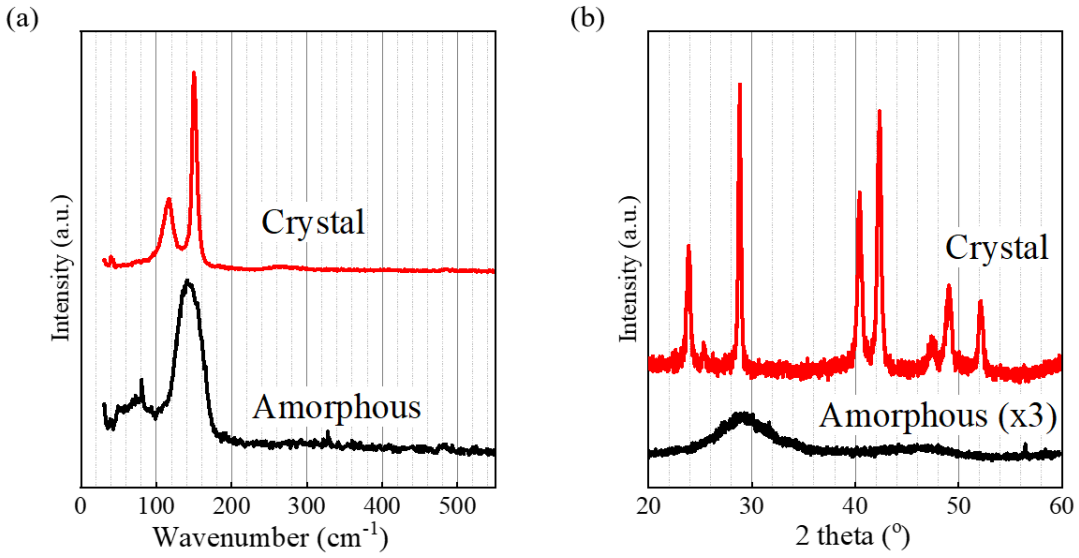

Supplementary Figure S10. Structural analysis (Raman and X-ray diffraction). (a) Raman spectroscopy. Raman results of crystalline AIST represent broader curve than those of crystalline AIST, owing to reduced stochasticity of local structures. The results are consistent with the precedent reports. [7] (b) X-ray diffraction (XRD). XRD results of crystalline AIST shows powder behaviour, while those of amorphous AIST shows bump at 28 degree. The results are consistent with the precedent reports. [4,8] For reference, crystal structure models of Sb_4Te(ST) and $AgInTe_2$ are specifically described.[9,10]

Reference

[1] T. Matsunaga, J. Akola, S. Kohara, T. Honma, K. Kobayashi, E. Ikenaga, R.O. Jones, N. Yamada, M. Takata, R. Kojima, From local structure to nanosecond recrystallization dynamics in AgInSbTe phase-change materials, Nat. Mater. 10 (2011) 129–134. https://doi.org/10.1038/nmat2931.

[2] T. Matsunaga, Y. Umetani, N. Yamada, Structural study of a Ag3.4In3.7Sb76.4Te16.5 quadruple compound utilized for phase-change optical disks, Phys. Rev. B - Condens. Matter Mater. Phys. 64 (2001) 184116-1–7. https://doi.org/10.1103/PhysRevB.64.184116.

[3] M. Zhu, W. Song, P.M. Konze, T. Li, B. Gault, X. Chen, J. Shen, S. Lv, Z. Song, M. Wuttig, R. Dronskowski, Direct atomic insight into the role of dopants in phase-change materials, Nat. Commun. 10 (2019) 1–10. https://doi.org/10.1038/s41467-019-11506-0.

[4] J. Singh, D.K. Aswal, S.K. Gupta, Annealing induced structural changes in sputtered AgInSbTe thin films and its implication on electrical properties, Mater. Res. Express. 2 (2015) 066403-1–8. https://doi.org/10.1088/2053-1591/2/6/066403.

[5] K. Shportko, S. Kremers, M. Woda, D. Lencer, J. Robertson, M. Wuttig, Resonant bonding in crystalline phase-change materials, Nat. Mater. 7 (2008) 653–658. https://doi.org/10.1038/nmat2226.

[6] T. Siegrist, P. Jost, H. Volker, M. Woda, P. Merkelbach, C. Schlockermann, M. Wuttig, Disorder-induced localization in crystalline phase-change materials, Nat. Mater. 10 (2011) 202–208. https://doi.org/10.1038/nmat2934.

[7] J. Tominaga, T. Kikukawa, M. Takahashi, R.T. Phillips, Structure of the optical phase change memory alloy, Ag-V-In-Sb-Te, determined by optical spectroscopy and electron diffraction, J. Appl. Phys. 82 (1997) 3214–3218. https://doi.org/10.1063/1.365627.

[8] M. Michler, A. Dommann, X-ray analytics of amorphous and crystalline phases of GST/AIST Phase Change Materials, Epcos.Org. (2014) 1–6. http://www.epcos.org/library/papers/pdf_2001/Michler.pdf.

[9] K. Kifune, T. Fujita, T. Tachizawa, Y. Kubota, N. Yamada, T. Matsunaga, Crystal structures of X-phase in the Sb-Te binary alloy system, Cryst. Res. Technol. 48 (2013) 1011–1021. https://doi.org/10.1002/crat.201300252.

[10] T. Kameyama, Y. Ishigami, H. Yukawa, T. Shimada, Y. Baba, T. Ishikawa, S. Kuwabata, T. Torimoto, Crystal phase-controlled synthesis of rod-shaped AgInTe2 nanocrystals for in vivo imaging in the near-infrared wavelength region, Nanoscale. 8 (2016) 5435–5440. https://doi.org/10.1039/c5nr07532g.